Phase Field Simulation of Dendritic Solidification of Ti-6Al-4V During Additive Manufacturing Process

Linmin Wu[1] and Jing Zhang[1,*]

[1]Department of Mechanical Engineering, Indiana University-Purdue University Indianapolis, Indianapolis, IN 46202, USA

*Email: jz29@iupui.edu; Phone: 317-278-7186; Fax:317-274-9744

Abstract

In this study, the phase field method is applied to simulate the phase transformation of Ti-6Al-4V from liquid phase to solid phase during solidification. The simulated results show the dendritic arms grow along the direction of the heat flow. Droplets are found formed inside dendrites. Solute enriches in the liquid near the dendritic tips and between dendritic arms. The effects of various processing parameters, including local temperature gradient, scan speed and cooling rate, on dendrites morphology and growth velocity are studied. The results show higher temperature gradient, scan speed and cooling rate will result in smaller dendritic arm spacing and higher growth velocity. The simulated dendritic morphology and arm spacings are in good agreement with experimental data and theoretical predictions.

Keywords: phase field; Ti-6Al-4V; temperature gradient; scan speed

---

This is the author's manuscript of the article published in final edited form as:

Wu, L., & Zhang, J. (2018). Phase Field Simulation of Dendritic Solidification of Ti-6Al-4V During Additive Manufacturing Process. JOM, 70(10), 2392–2399. https://doi.org/10.1007/s11837-018-3057-z

1. Introduction

Additive manufacturing has drawn widespread attentions because it has several advantages compared with conventional manufacturing, such as easier to fabricate complex geometry, optimum material usage and saving expensive tools cost [1-3]. Laser powder bed fusion is one of the additive manufacturing techniques, which manufactures metallic parts in a short time and high precision [4, 5]. Laser powder bed fusion uses high energy power source to melt the powders and build the parts in a layer by layer fashion. During the process, solidification and phase transformation occur in the melt pool [6, 7] due to the cooling. This will significantly affect the material properties of the fabricated parts, since solidification controls the morphology of the microstructure. Thus, it is essential to understand the solidification behavior during the fabrication.

In additive manufacturing, two main solidification parameters are dendritic arm spacing and microsegregation. The distribution and the spacing of dendritic arms are related to mechanical properties, such as tensile strength and ultimate tensile strength [8-10]. Microsegregation, caused by non-equilibrium partition of solute in solid and liquid, affects the texture of dendrites. Depending on the directions of the temperature gradient, the orientations of dendrites will lead to anisotropic mechanical properties. It is important to understand the mechanical properties of additive manufactured part by investigating dendritic arm spacing and microsegregation.

Titanium based alloys, especially Ti-6Al-4V, are widely used in aerospace, biomedical and automotive industries due to their excellent mechanical strength and creep resistance at high temperatures [11-13]. Recently, many studies were carried out to investigate the microstructures and material properties of laser deposited Ti-6Al-4V by experiments [14-18]. However, due to the short time scale of the solidification and the small length scale of the melting pool, it is very difficult to study the microstructure evolution during the fabrication process by experiment. Hence,

numerical simulations aiming to reveal microstructure evolution during the solidification process are warranted.

Different numerical methods have been developed to study the dendritic growth during solidification. Among them, cellular automaton and phase field method have been used extensively. Cellular automaton method has been applied to simulate the dendrites formation during solidification [19-22]. Due to its low computational cost, it can be used to simulate microstructure evolution in large systems [23, 24]. However, artificial anisotropy may be introduced by the cellular automaton mesh, which has been reported in [25-27]. Phase field method is a promising technique to describe the microstructure evolution [28-30]. It has been used to simulate the dendrites growth in undercooled pure materials [31, 32], and has been extended to describe the dendrites morphology in binary alloys [33-36]. Compared with cellular automaton, phase field method can capture more physics phenomenon during solidification process, like pore formation [37, 38]. For Ti-6Al-4V, only few studies have been carried out by phase field method. Gong and Chou [39] applied phase field method to investigate the columnar grain growth of Ti-6Al-4V during solidification and compared grain sizes with experimental results. Sahoo and Chou [40] studied the dendritic arm spacing with different processing parameters in electron beam additive manufactured Ti-6Al-4V. In this study, the phase field method will be employed to simulate the phase transformation from liquid phase to solid prior β phase of Ti-6Al-4V during rapid solidification. The influence of the local temperature gradient, scan speed and cooling rate will be investigated.

The paper is organized as follows: In section 2, the details of model formulations describing phase evolution and mass transport will be given. In section 3, the effects of different solidification conditions, including temperature gradient, scan speed and cooling rate, on dendritic morphology

will be studied. Comparison of simulated results with experimental observations and theoretical predictions will be discussed. Conclusions are given in section 4.

2. Model description

To simulate the microstructure evolution of Ti-6Al-4V during additive manufacturing process, phase field method is employed. In a ternary system, if an element doesn't have the concentration gradient and two other elements diffuse, the system can be simplified as a binary system. In this study, Ti-6Al-4V is assumed pseudo-binary alloy, and the solute is the mixture of Al and V. It is shown that the pseudo-binary approach can be a successful replacement for the multi-component approach when simulating the solidification of Ti-base alloy such as Ti-6Al-4V [41, 42]. Followed by Echebarria *et al*. [35] and Ramirez *et al*. [36], a quantitative binary alloy model is used. The model was developed based on thin interface limit and has the following assumptions: (1) The effects of convection are not considered, and the mass transport is governed by diffusion; (2) Thermal-physical properties are considered constant; (3) The effect of latent heat of fusion is neglected and frozen temperature approximation is used.

The phase field simulations are carried out to simulate the phase transformation from liquid phase to solid prior β phase. The model consists of two coupled equations, with one describing the evolution of phase order parameter φ, and the other governs the mass transport of the composition c during the solidification of a binary alloy. The dimensionless forms of governing equations are given by,

$$a(\theta)^2 \frac{\partial \varphi}{\partial t} = \nabla \cdot \left[a(\theta)^2 \nabla \varphi \right] - \frac{\partial}{\partial x}\left[a(\theta) \frac{\partial a(\theta)}{\partial \theta} \frac{\partial \varphi}{\partial y} \right] + \frac{\partial}{\partial y}\left[a(\theta) \frac{\partial a(\theta)}{\partial \theta} \frac{\partial \varphi}{\partial x} \right] + \varphi - \varphi^3 - \lambda\left(1-\varphi^2\right)^2 \left[U + \frac{T - T_0}{m_l c_0 (1-k)/k} \right] \tag{1}$$

$$\frac{\partial c}{\partial t} = \nabla \cdot \left[D \frac{1-\varphi}{1+k-(1-k)\varphi} \nabla u \right] + \nabla \cdot j_{at} \tag{2}$$

where φ is phase order parameter with $\varphi = -1$ representing solid phase and $\varphi = 1$ meaning liquid phase. $a(\theta) = 1 + \varepsilon \cos(4\theta)$ represents the four-fold surface energy anisotropy at the solid-liquid interface with the strength of anisotropy ε and the angle between the interface normal and the x direction $\theta = \arctan\left(\partial_y \varphi / \partial_x \varphi\right)$. $k = c_s / c_l$ is partition coefficient, where c_s and c_l are equilibrium compositions on solid and liquid side of the interface, respectively. m_l is liquidus slope and c_0 is alloy concentration far from the solidification front. U is the dimensionless supersaturation, which is defined as, $U = \left(e^u - 1\right)/(1-k)$, where u is a dimensionless chemical potential given by,

$$u = \ln\left(\frac{2ck / c_0}{1+k-(1-k)\varphi} \right) \tag{3}$$

The frozen temperature approximation is applied to the system, which is described by $T = T_0 + G(y - Vt)$. G and V are temperature gradient and constant pulling speed along y direction, respectively. T_0 is the reference temperature.

In equation (2), $D = D_l(1-\varphi)/2 + D_s(1+\varphi)/2$ is diffusion coefficient of the system, where D_l and D_s are diffusion coefficient in liquid and solid phase, respectively. The anti-

trapping current j_{at} was introduced to the diffusion equation to suppress the solute-trapping effects at the solid-liquid interface [35], and is given by,

$$j_{at} = \frac{1}{2\sqrt{2}} U \frac{\partial \varphi}{\partial t} \hat{n} \tag{4}$$

where $\hat{n} = -\nabla\varphi / |\nabla\varphi|$ is the unit vector normal to the solid-liquid interface.

There are three characteristic parameters in the phase field model, the characteristic length W, the characteristic time τ and the coupling constant λ. Based on thin interface analysis, two equations are given to describe the relationship of these three parameters,

$$\lambda = \frac{a_1 W}{d} \tag{5}$$

$$\tau = \frac{a_2 \lambda W^2}{D_l} \tag{6}$$

where d is the chemical capillary length. $a_1 = 0.8839$ and $a_2 = 0.6267$ are constant, which is given in [35].

To solve the phase field equation (1) and the mass transport equation (2), a finite volume method is used with explicit time marching. No flux boundary conditions were applied on all boundaries. A uniform square mesh 300 x 300 grid points is used. The grid spacing is set as $dx = dy = 0.04$ μm and the time step $dt = 0.02$ μs is used. The characteristic length $W = 0.1$ μm is chosen. Other parameter values are listed in Table I. Each simulation is initialized with a thin layer of solid with a height of 0.03 μm at the bottom of the domain. Small random fluctuations are applied on the interface. The initial concentration is set as c_0 in the solid and kc_0 in the liquid. For

simulations, different processing parameters, the temperature gradient G and the scan speed V are used. The effects of processing parameters on microstructure evolution of Ti-6Al-4V will be discussed in the following section.

Table I: Material properties used in the simulations [39-41]

Initial alloy concentration c_0	10%
Partition coefficient k	0.5
Liquidus slope m_l	-0.088 K/%
Liquidus temperature T_l	1928 K
Solidus temperature T_s	1878 K
Liquid diffusion coefficient D_l	9.5×10^{-9} m^2/s
Solid diffusion coefficient D_s	5×10^{-13} m^2/s
Anisotropy strength ε	0.05
Gibbs-Thomson coefficient Γ	1.88×10^{-7} K m

3. Results and discussion

The simulated microstructure evolution of Ti-6Al-V during solidification is shown in Fig. 1 and Fig. 2. Three features can be observed from the structures. First, the microstructure shows columnar structures. With the increase of solidification time, the initial random nuclei become unstable and start to grow. Finally, parallel dendritic arms are formed. The growth of the dendritic arms is along the direction of the heat flow, which is in y-direction in this case. Second, droplets are formed inside dendrites during the solidification. These droplets have high solute

concentration. Similar results are found in the rapid solidification process of binary alloys [43, 44]. Third, there is significant micro-segregation phenomenon. It is found that solute enriches in the liquid near the dendritic tips and between dendritic arms. As the dendritic arms grow, the liquid concentration increases near the tip regions and decreases rapidly to the alloy concentration far away from the solidification front c_0. In Fig. 3, SEM image of electron beam additive manufactured Ti-6Al-4V sample is shown. It can be seen from the microstructure that columnar dendritic structures are formed, which is columnar prior β grains. The phase field simulations were carried out to simulate the phase transformation from liquid phase to solid prior β phase. The simulated phase and solute concentration profiles are comparable with the experimental observations.

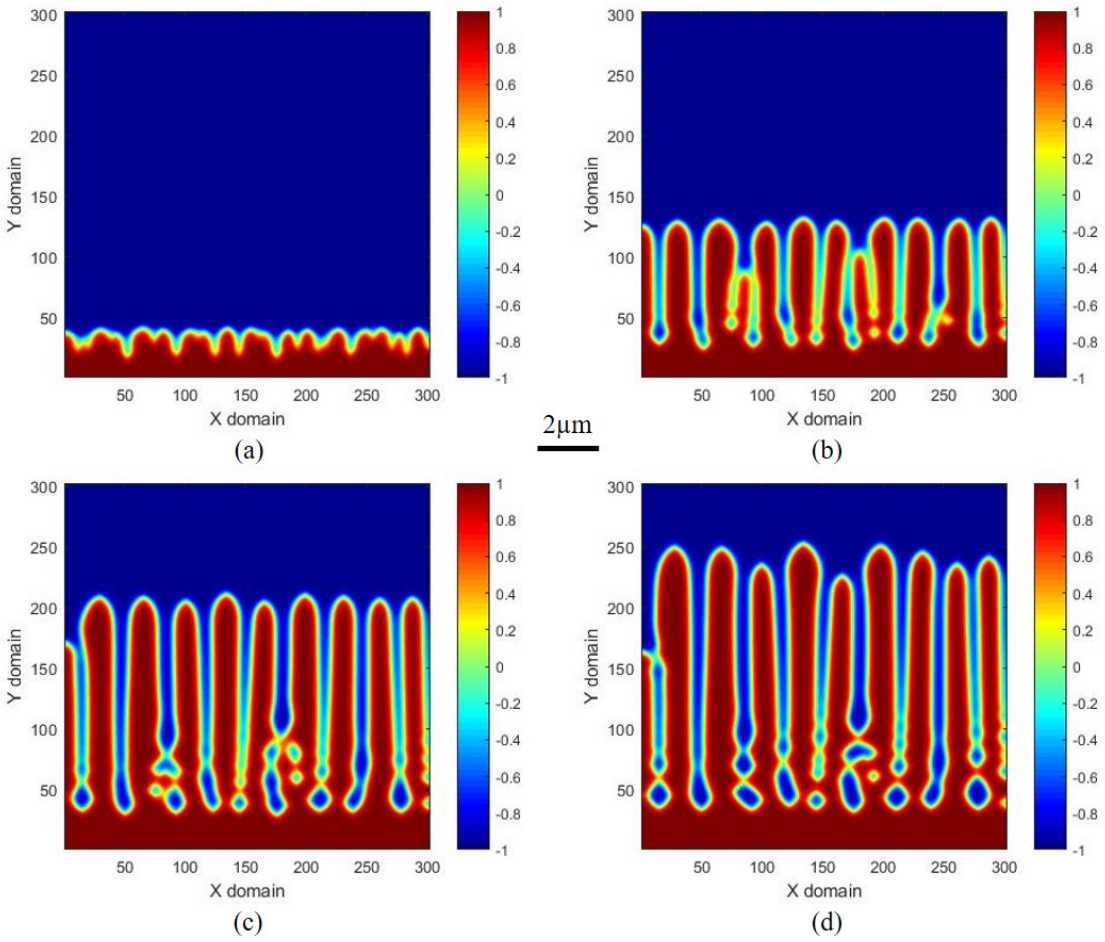

Fig. 1 Simulated columar structure at different times with $G = 2800$ K/mm and $V = 400$ mm/s. (a) 0.02 ms, (b) 0.1 ms, (c) 0.2 ms, (d) 0.3 ms.

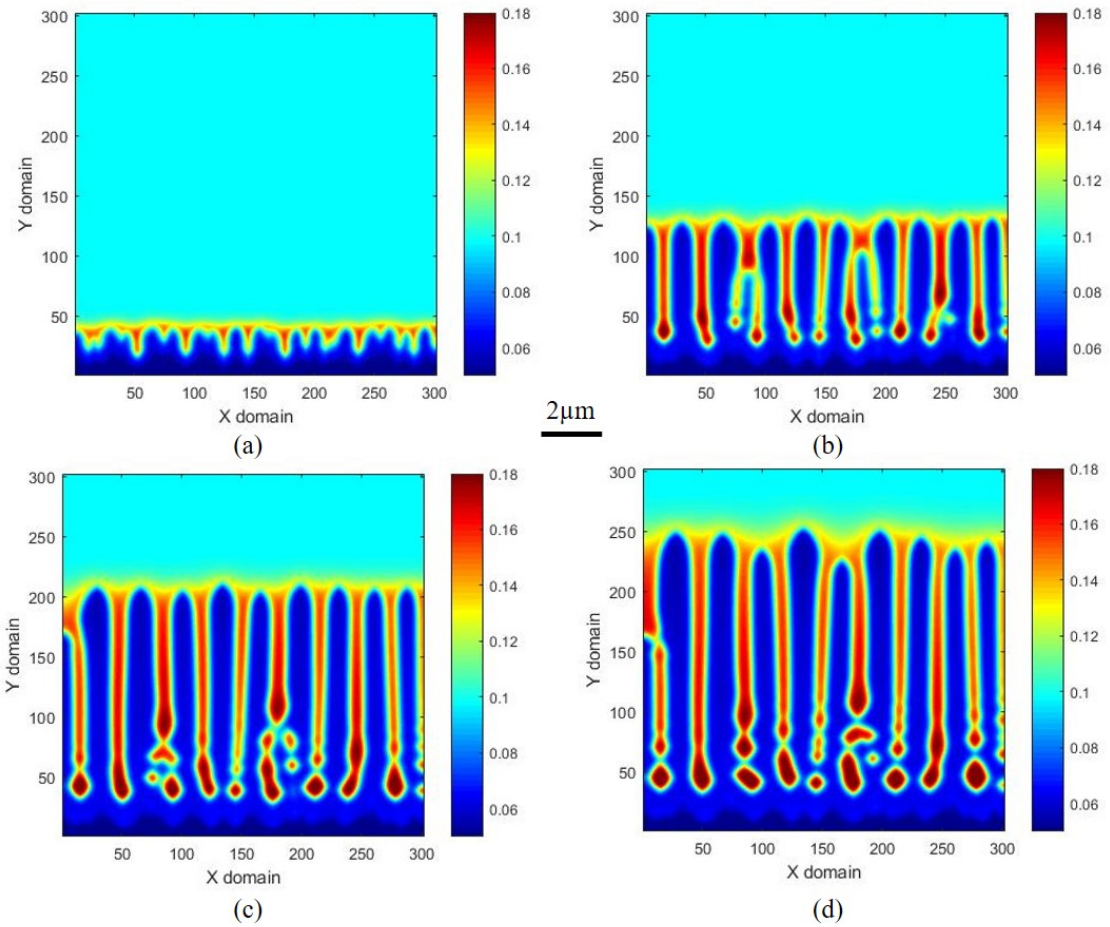

Fig. 2 Simulated solute concentration at different times with $G = 2800$ K/mm and $V = 400$ mm/s. (a) 0.02 ms, (b) 0.1 ms, (c) 0.2 ms, (d) 0.3 ms.

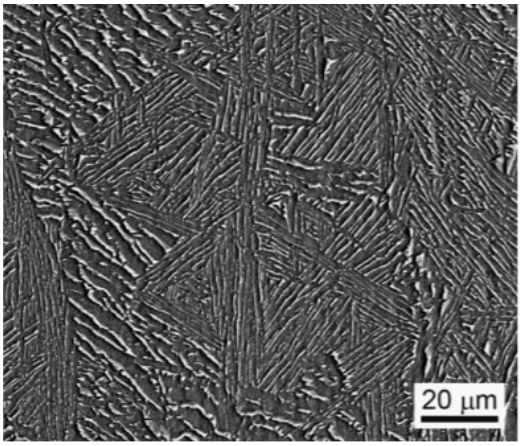

Fig. 3 SEM image of electron beam additive manufactured Ti-6Al-4V sample. Reprinted with permission from reference [45].

One important parameter used to quantify the microstructure after solidification is Primary Dendritic Arm Spacing (PDAS). Broderick *et al*. [46] investigated the effects of cooling conditions on the microstrucutre of rapidly solidified Ti-6Al-4V experimentally. The correlation between cooling rate $\dot{T}$ and PDAS is given by,

$$PDAS = A(GV)^n = A\dot{T}^n \tag{7}$$

where A and n are constants. After fitting to the experimental data, A and n are obtained as 3.1×10^6 μm $(K/s)^{1.05}$ and -1.05. In order to compare the simulation results with the experimental values, phase field simulations with constant scan speed 400 mm/s and different temperture gradient varying from 2000 K/mm to 2800 K/mm were carried out. The comparison is shown in Fig. 4. In overall, the simulated PDAS is in agreement with the experimental fitted values. It can be seen that PDAS reduces with the increasing cooling rate, implying that higher cooling rate will results in a finer columnar structure during solidification.

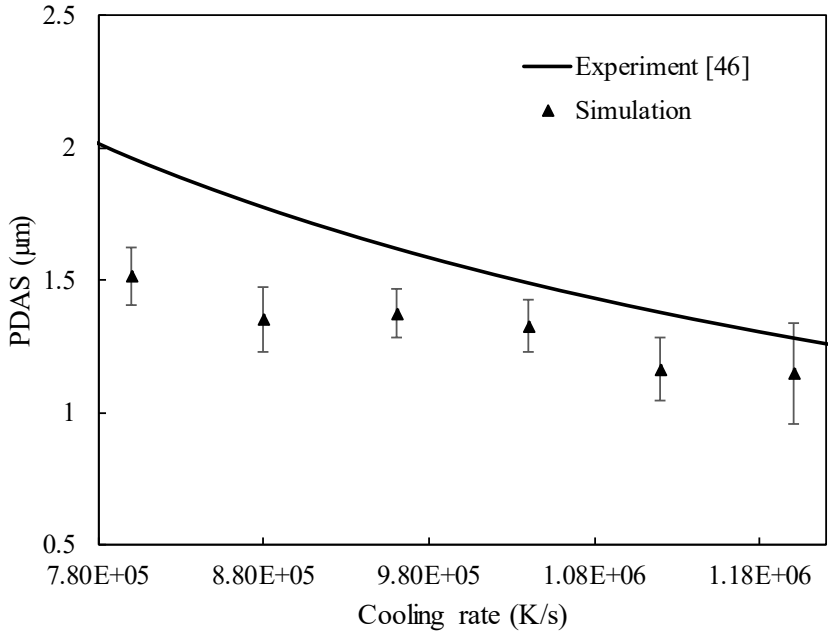

Fig. 4 Comparison of simulated PDAS values with experimental fitted results.

To study the effect of temperature gradient on microstructure, simulations with a fixed scanning speed 400mm/s and different temperature gradient were performed. The microstructure of simulated results is shown in Fig. 5. It can be seen that with the increase of the temperature gradient, the columnar structure become denser, indicating smaller PDAS. Besides, the growth velocity of the dendrites is higher when temperature gradient is larger. This result is consistent with the previous experimental data, as elavated temperature gradient means higher cooling rate. The simulated PDAS is also compared with analytical models. Hunt [47] proposed a theoretial model to predict PDAS by considering the geometry of dendrite tip. The model is given by,

$$PDAS = 2.83\left(k\Gamma\Delta T_0 D_l\right)^{0.25} G^{-0.5} V^{-0.25} \tag{8}$$

where Γ is Gibbs-Thompson coefficient and ΔT_0 is equilibrium freezing range. Kurz and Fisher [48] improved the model by considering the entire geometry, including dendrite tip and trunk. The Kurz and Fisher model is expressed by,

$$PDAS = 4.3\left(k\Gamma\Delta T_0 D_l\right)^{0.25} G^{-0.5} V^{-0.25} \tag{8}$$

The comparison is shown in Fig. 6. For simulated PDAS, with the increase of temperature gradient from 2000 K/mm to 3000 K/mm, the PDAS decreases from 1.52 μm to 1.15 μm. It can be obtained that the simulated PDAS lies between the Hunt's and Kurz's results. In general, the simulated PDAS has the same trend as Hunt's and Kurz's models. The differences of the simulated results and theoretical predictions may be caused by the following reasons. First, the theoretical models were developed based on three-dimensional cases, while the phase field simulations were carried out in two dimension. Second, both models assumes the initial conditions as simple geometry, meanwhile small random pertubations were used as initial conditions in this study.

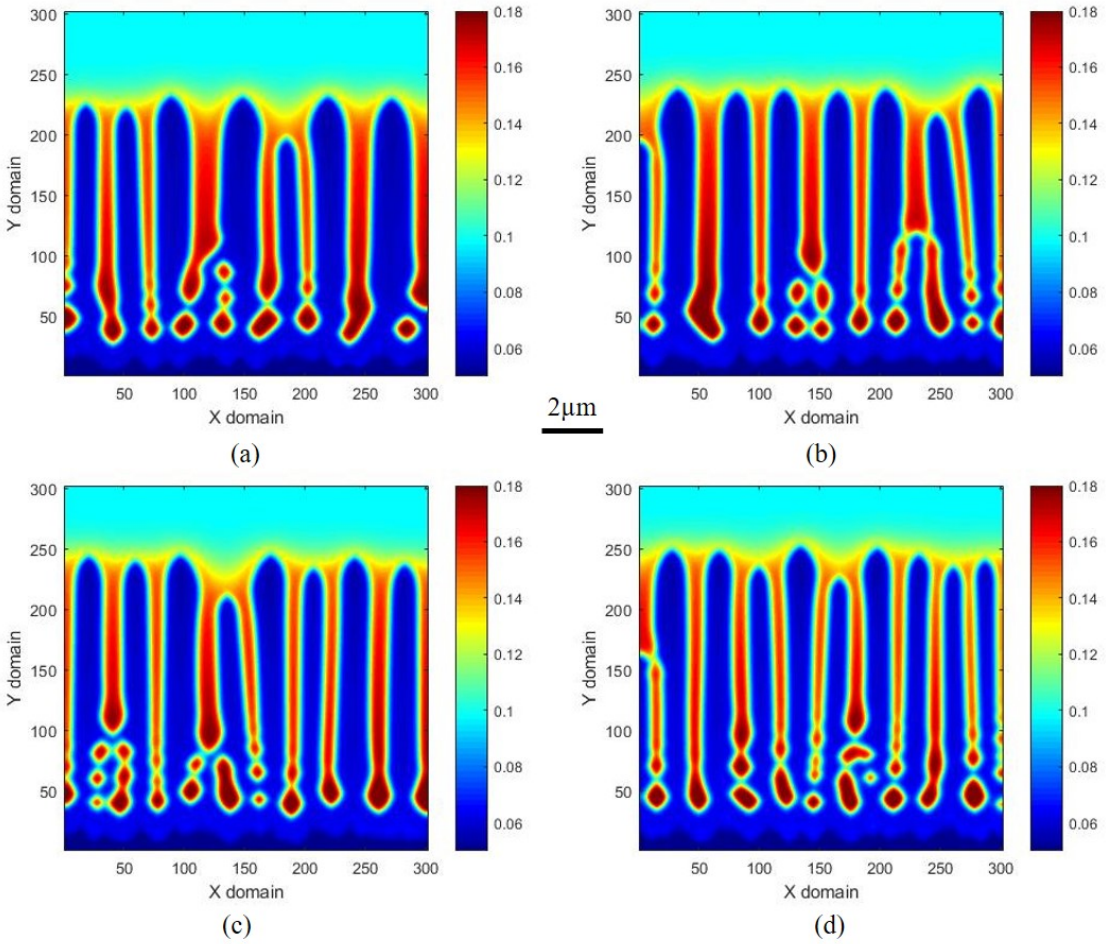

Fig. 5 Simulated solute concentration at 0.3 ms with $V = 400$ mm/s and, (a) $G = 2200$ K/mm, (b) $G = 2400$ K/mm, (c) $G = 2600$ K/mm, (d) $G = 2800$ K/mm.

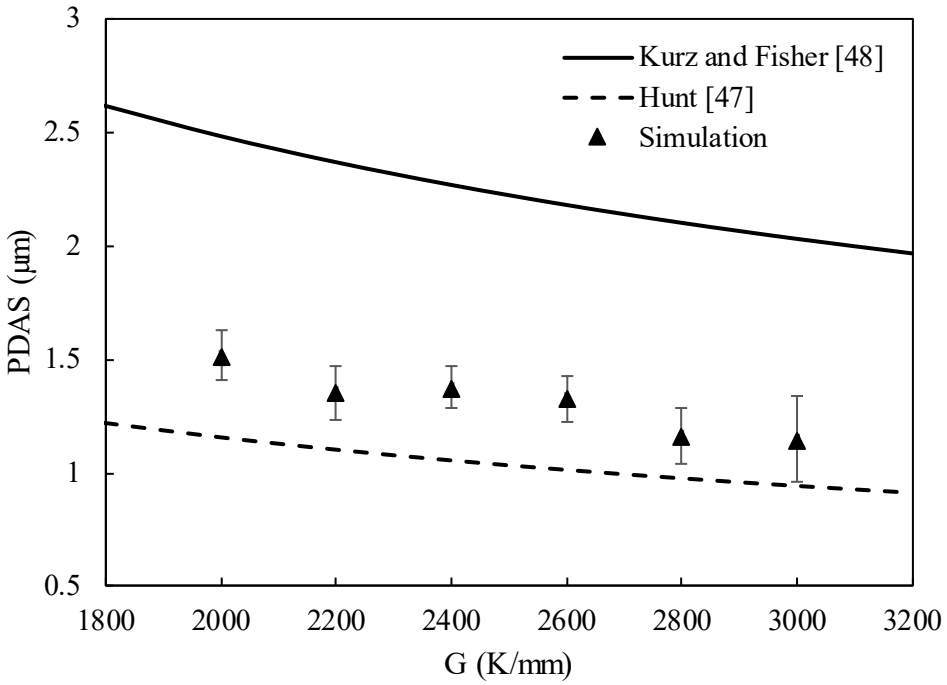

Fig. 6 Comparison of simulated PDAS with theoretical predictions. The scan speed is fixed at 400 mm/s.

The effect of scan speed on Ti-6Al-4V was studied by fixing the temperature gradient at 2000 K/mm and varing the scan speed from 200 mm/s to 800 mm/s. The simulated solute concentration profile is shown in Fig. 7. It can be observed that the effect of increasing scan speed is simmilar to increasing temperature gradient, as both of them increase the cooling rate. With the increase of the scan speed, finer columnar morphology and higher growth velocity is observed. The comparision of the simulated PDAS with the theoretial predictions is plotted in Fig. 8. For simulation results, as the increase of scan speed from 200 mm/s to 800 mm/s, the PDAS decreases from 1.58 μm to 1.36 μm, which is comparable with analytical model results.

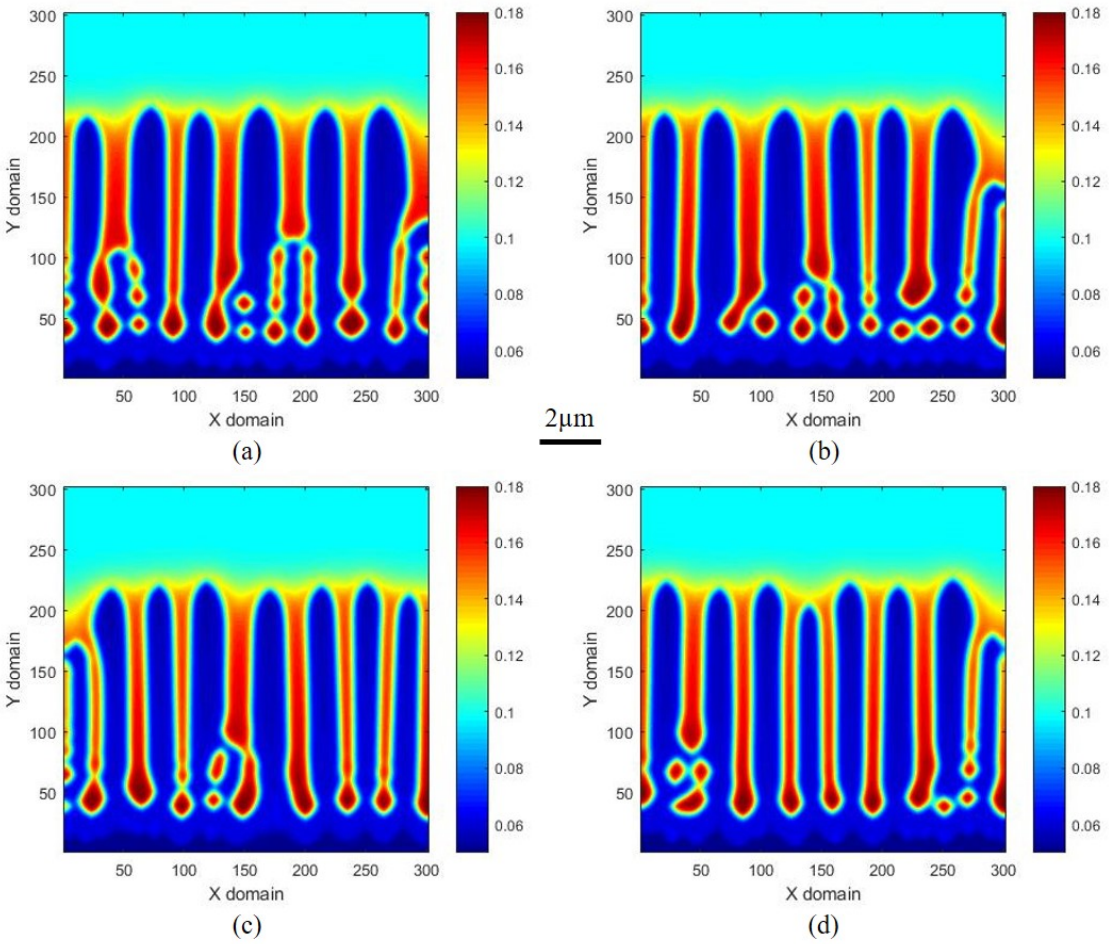

Fig. 7 Simulated solute concentration at 0.3 ms with $G = 2000$ K/mm and, (a) $V = 200$ mm/s, (b) $V = 400$ mm/s, (c) $V = 600$ mm/s, (d) $V = 800$ mm/s.

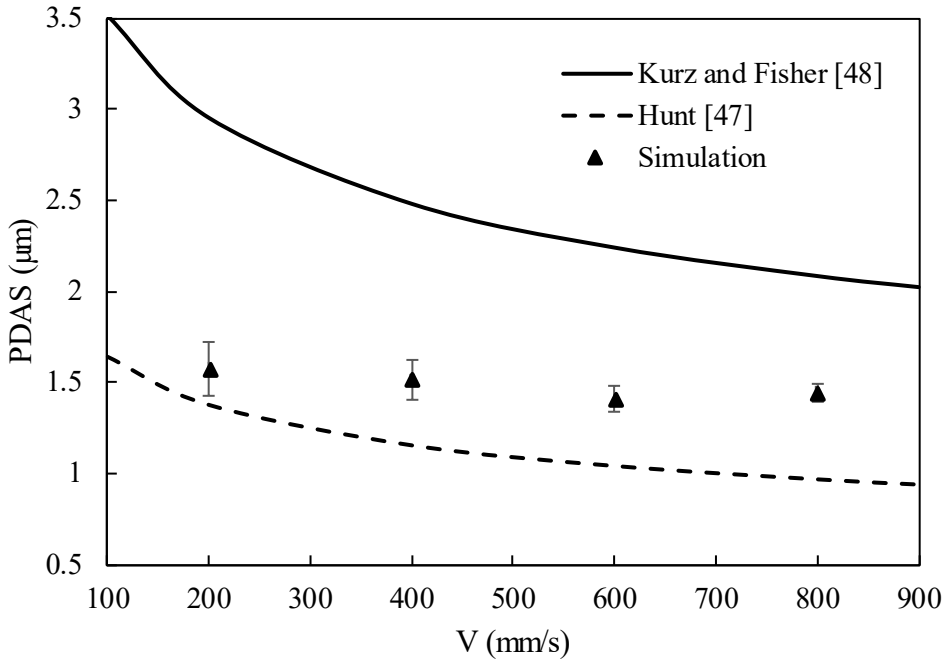

Fig. 8 Comparison of simulated PDAS with theoretical predictions. The temperature gradient is fixed at 2000 K/mm.

4. Conclusions

A phase field model was developed to simulate the dendritic solidification of Ti-6Al-4V alloy during additive manufacturing process. The dendrites morphology, microsegregation, as well as primary arm spacing are discussed under different laser scan speed and temperature gradient. This study shows phase field method can be used as a tool to simulate the additive manufacturing process. The major conclusions are summarized as follows:

(1) The phase field method can simulate the phase transformation from liquid phase to solid phase of Ti-6Al-4V during solidification. The morphology shows columnar structure.

(2) The growth of the dendritic arms is along the direction of the heat flow.

(3) Microsegregation phenomenon is observed during dendrites formation. It is found that solute enriches in the liquid near the dendritic tips and between dendritic arms.

(4) Scan speed has influence on dendrites morphology. By increasing scan speed from 200 mm/s to 800 mm/s, the primary arm spacing decreases from 1.58 μm to 1.36 μm.

(5) With the increase of temperature gradient from 2000 K/mm to 3000 K/mm, the primary arm spacing decreases from 1.52 μm to 1.15 μm.

(6) The primary arm spacing results obtained by phase field simulation are in good agreement with experimental data and analytical predictions.

List of Figures

List of Tables

References

1. K. V. Wong and A. Hernandez, A Review of Additive Manufacturing, *ISRN Mechanical Engineering*, 2012(2012).
2. D. L. Bourell, Perspectives on Additive Manufacturing, *Annual Review of Materials Research*, 46(2016), No.1.
3. Y. Zhang, L. Wu, X. Guo, S. Kane, Y. Deng, Y.-G. Jung, J.-H. Lee and J. Zhang, Additive Manufacturing of Metallic Materials: A Review, *Journal of Materials Engineering and Performance*, 27(2018), No.1.
4. W. E. King, A. T. Anderson, R. M. Ferencz, N. E. Hodge, C. Kamath, S. A. Khairallah and A. M. Rubenchik, Laser Powder Bed Fusion Additive Manufacturing of Metals: Physics, Computational, and Materials Challenges, *Applied Physics Reviews*, 2(2015), No.4.
5. W. E. Frazier, Metal Additive Manufacturing: A Review, *Journal of Materials Engineering and Performance*, 23(2014), No.6.
6. L. E. Murr, S. M. Gaytan, D. A. Ramirez, E. Martinez, J. Hernandez, K. N. Amato, P. W. Shindo, F. R. Medina and R. B. Wicker, Metal Fabrication by Additive Manufacturing Using Laser and Electron Beam Melting Technologies, *Journal of Materials Science & Technology*, 28(2012), No.1.
7. H. L. Wei, J. Mazumder and T. DebRoy, Evolution of Solidification Texture during Additive Manufacturing, *Scientific Reports*, 5(2015).
8. W. R. Osorio, P. R. Goulart, A. Garcia, G. A. Santos and C. M. Neto, Effect of dendritic arm spacing on mechanical properties and corrosion resistance of Al 9 Wt Pct Si and Zn 27 Wt Pct Al alloys, *Metallurgical and Materials Transactions A*, 37(2006), No.8.
9. K. S. Cruz, E. S. Meza, F. A. P. Fernandes, J. M. V. Quaresma, L. C. Casteletti and A. Garcia, Dendritic Arm Spacing Affecting Mechanical Properties and Wear Behavior of Al-Sn and Al-Si Alloys Directionally Solidified under Unsteady-State Conditions, *Metallurgical and Materials Transactions A*, 41(2010), No.4.
10. Y. Ruan, A. Mohajerani and M. Dao, Microstructural and Mechanical-Property Manipulation through Rapid Dendrite Growth and Undercooling in an Fe-based Multinary Alloy, *Scientific Reports*, 6(2016).
11. S. Zherebtsov, G. Salishchev, R. Galeyev and K. Maekawa, Mechanical Properties of Ti-6Al-4V Titanium Alloy with Submicrocrystalline Structure Produced by Severe Plastic Deformation, *Materials Transactions*, 46(2005), No.9.
12. C. Qiu, N. J. E. Adkins and M. M. Attallah, Microstructure and tensile properties of selectively laser-melted and of HIPed laser-melted Ti–6Al–4V, *Materials Science and Engineering: A*, 578(2013).
13. T. Vilaro, C. Colin and J. D. Bartout, As-Fabricated and Heat-Treated Microstructures of the Ti-6Al-4V Alloy Processed by Selective Laser Melting, *Metallurgical and Materials Transactions A*, 42(2011), No.10.
14. H. Galarraga, D. A. Lados, R. R. Dehoff, M. M. Kirka and P. Nandwana, Effects of The Microstructure and Porosity on Properties of Ti-6Al-4V Alloy Fabricated by Electron Beam Melting (EBM), *Additive Manufacturing*, 10(2016).
15. N. Hrabe and T. Quinn, Effects of Processing on Microstructure and Mechanical Properties of A Titanium Alloy (Ti–6Al–4V) Fabricated Using Electron Beam Melting

(EBM), Part 1: Distance from Build Plate and Part Size, *Materials Science and Engineering: A*, 573(2013).
16. N. Hrabe and T. Quinn, Effects of processing on microstructure and mechanical properties of a titanium alloy (Ti–6Al–4V) fabricated using electron beam melting (EBM), Part 2: Energy input, orientation, and location, *Materials Science and Engineering: A*, 573(2013).
17. F. Luca, M. Emanuele, R. Pierfrancesco and M. Alberto, Microstructure and Mechanical Properties of Ti‐6Al‐4V Produced by Electron Beam Melting of Pre‐Alloyed Powders, *Rapid Prototyping Journal*, 15(2009), No.3.
18. Q. Liu, Y. Wang, H. Zheng, K. Tang, L. Ding, H. Li and S. Gong, Microstructure and mechanical properties of LMD–SLM hybrid forming Ti6Al4V alloy, *Materials Science and Engineering: A*, 660(2016).
19. M. F. Zhu and D. M. Stefanescu, Virtual front tracking model for the quantitative modeling of dendritic growth in solidification of alloys, *Acta Materialia*, 55(2007), No.5.
20. L. Beltran-Sanchez and D. M. Stefanescu, Growth of solutal dendrites: A cellular automaton model and its quantitative capabilities, *Metallurgical and Materials Transactions A*, 34(2003), No.2.
21. M. F. Zhu, S. Y. Lee and C. P. Hong, Modified cellular automaton model for the prediction of dendritic growth with melt convection, *Physical Review E*, 69(2004), No.6.
22. C. Shaohua, X. Yaopengxiao and J. Yang, A hybrid finite-element and cellular-automaton framework for modeling 3D microstructure of Ti–6Al–4V alloy during solid–solid phase transformation in additive manufacturing, *Modelling and Simulation in Materials Science and Engineering*, 26(2018), No.4.
23. M. Asle Zaeem, H. Yin and S. D. Felicelli, Modeling dendritic solidification of Al–3%Cu using cellular automaton and phase-field methods, *Applied Mathematical Modelling*, 37(2013), No.5.
24. B. Jelinek, M. Eshraghi, S. Felicelli and J. F. Peters, Large-scale parallel lattice Boltzmann–cellular automaton model of two-dimensional dendritic growth, *Computer Physics Communications*, 185(2014), No.3.
25. Y. Hebi and D. F. Sergio, A cellular automaton model for dendrite growth in magnesium alloy AZ91, *Modelling and Simulation in Materials Science and Engineering*, 17(2009), No.7.
26. M. J. M. Krane, D. R. Johnson and S. Raghavan, The development of a cellular automaton-finite volume model for dendritic growth, *Applied Mathematical Modelling*, 33(2009), No.5.
27. G. S. Grest, D. J. Srolovitz and M. P. Anderson, Computer simulation of grain growth—IV. Anisotropic grain boundary energies, *Acta Metallurgica*, 33(1985), No.3.
28. N. Moelans, B. Blanpain and P. Wollants, Quantitative Analysis of Grain Boundary Properties in A Generalized Phase Field Model For Grain Growth in Anisotropic Systems, *Physical Review B*, 78(2008), No.2.
29. L. Wu, Y. Zhang, Y.-G. Jung and J. Zhang, Three-dimensional phase field based finite element study on Li intercalation-induced stress in polycrystalline LiCoO2, *Journal of Power Sources*, 299(2015).
30. N. Moelans, B. Blanpain and P. Wollants, An Introduction to Phase-Field Modeling of Microstructure Evolution, *Calphad*, 32(2008), No.2.

31. A. F. Ferreira, A. J. d. Silva and J. A. d. Castro, Simulation of The Solidification of Pure Nickel via The Phase-Field Method, *Materials Research*, 9(2006).
32. R. Kobayashi, Phase Field Simulations of Dendritic Solidification, *Advanced Materials* (1994), 529-532.
33. S. G. Kim, W. T. Kim and T. Suzuki, Phase-Field Model for Binary Alloys, *Physical Review E*, 60(1999), No.6.
34. Z. Bi and R. F. Sekerka, Phase-Field Model of Solidification of A Binary Alloy, *Physica A: Statistical Mechanics and its Applications*, 261(1998), No.1.
35. B. Echebarria, R. Folch, A. Karma and M. Plapp, Quantitative Phase-Field Model of Alloy Solidification, *Physical Review E*, 70(2004), No.6.
36. J. C. Ramirez, C. Beckermann, A. Karma and H. J. Diepers, Phase-Field Modeling of Binary Alloy Solidification with Coupled Heat and Solute Diffusion, *Physical Review E*, 69(2004), No.5.
37. H. Meidani and A. Jacot, Phase-field simulation of micropores constrained by the dendritic network during solidification, *Acta Materialia*, 59(2011), No.8.
38. T. Keller, G. Lindwall, S. Ghosh, L. Ma, B. M. Lane, F. Zhang, U. R. Kattner, E. A. Lass, J. C. Heigel, Y. Idell, M. E. Williams, A. J. Allen, J. E. Guyer and L. E. Levine, Application of finite element, phase-field, and CALPHAD-based methods to additive manufacturing of Ni-based superalloys, *Acta Materialia*, 139(2017).
39. X. Gong and K. Chou, Phase-Field Modeling of Microstructure Evolution in Electron Beam Additive Manufacturing, *JOM*, 67(2015), No.5.
40. S. Sahoo and K. Chou, Phase-Field Simulation of Microstructure Evolution of Ti–6Al–4V in Electron Beam Additive Manufacturing Process, *Additive Manufacturing*, 9(2016).
41. L. Nastac, J. Valencia, J.Xu and H. Dong, Assessment of Solidification-Kinetics Parameters for Titanium-Base Alloys, *Proceedings of the International Symposium on Liquid Metals Processing and Casting*(1999).
42. L. Nastac, Solute Redistribution, Liquid/Solid Interface Instability, and Initial Transient Regions during the Unidirectional Solidification of Ti-6-4 and Ti-17 Alloys, *CFD Modeling and Simulation in Materials Processing*, (2012), 123-130.
43. G. Supriyo, M. Li, O.-O. Nana and E. G. Jonathan, On The Primary Spacing and Microsegregation ff Cellular Dendrites in Laser Deposited Ni–Nb Alloys, *Modelling and Simulation in Materials Science and Engineering*, 25(2017), No.6.
44. V. Fallah, M. Amoorezaei, N. Provatas, S. F. Corbin and A. Khajepour, Phase-Field Simulation of Solidification Morphology in Laser Powder Deposition of Ti–Nb Alloys, *Acta Materialia*, 60(2012), No.4.
45. H. K. Rafi, N. V. Karthik, H. Gong, T. L. Starr and B. E. Stucker, Microstructures and Mechanical Properties of Ti6Al4V Parts Fabricated by Selective Laser Melting and Electron Beam Melting, *Journal of Materials Engineering and Performance*, 22(2013), No.12.
46. T. F. Broderick, A. G. Jackson, H. Jones and F. H. Froes, The Effect of Cooling Conditions on The Microstructure of Rapidly Solidified Ti-6Al-4V, *Metallurgical Transactions A*, 16(1985), No.11.
47. M. H. Burden and J. D. Hunt, Cellular and Dendritic Growth. I, *Journal of Crystal Growth*, 22(1974), No.2.
48. W. Kurz and D. J. Fisher, Dendrite Growth at The Limit of Stability: Tip Radius and Spacing, *Acta Metallurgica*, 29(1981), No.1.